THE JOURNAL OF PHYSICAL CHEMISTRY C
A JOURNAL OF THE AMERICAN CHEMICAL SOCIETY

pubs.acs.org/JPCC

Article

Enhancing Lithium Iron Phosphate as a Cathode Material by Codoping with Nickel and Silicon: A First-Principles Study

Yelak F. Abebe, Arindam Sannyal, Kisang Byun, Mengdi Zhao,* and Joonkyung Jang*

Cite This: *J. Phys. Chem. C* 2026, 130, 5369−5377

Read Online

ACCESS | Metrics & More | Article Recommendations | Supporting Information

ABSTRACT: Lithium iron phosphate (LFP) is a cost-effective cathode material with thermal stability but limited high-rate performance because of the intrinsic two-phase (de)lithiation mechanism and concomitant sluggish phase-boundary propagation during cycling. Herein, density functional theory calculations are employed to investigate the effect of doping with Ni and Si on the phase stability, structural evolution, and electrochemical characteristics of LFP. Codoping LFP with Ni and Si uniquely introduced multiple thermodynamically stable intermediate phases throughout the entire (de)lithiation process, replacing the single two-phase reaction of pristine LFP with sequential two-phase transitions. Ni and Si codoping also improved structural integrity and intercalation voltage during cycling. Moreover, codoping reduced the electronic band gap, thereby enhancing electronic transport in LFP.

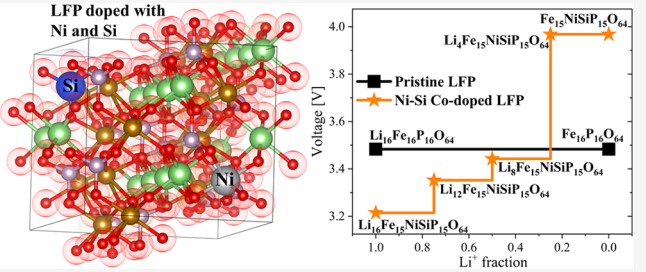

1. INTRODUCTION

Lithium-ion batteries (LIBs) currently offer the highest efficiencies for electrochemical energy storage applications. Nevertheless, to meet the ever-growing demands for large-scale energy storage systems, such as electric vehicles and grids, further enhancements in LIB efficiency and capacity are required. The cathode material *lithium iron phosphate* (LFP; $LiFePO_4$) has been extensively studied and utilized because of its high reversible capacity, excellent thermal stability, environmental compatibility, and affordability. Despite these advantages, LFP suffers from intrinsically poor electronic and ionic conductivities, which significantly hinder its widespread applications.[1−4] The low electronic conductivity originates from a strong localization of Fe 3d electrons and the polyanionic PO_4^{3-} framework that limit electronic band dispersion and provide a wide band gap. The slow ionic transport of Li is attributed to the one-dimensional channel along the [010] direction that induces sluggish ionic conductivity. Consequently, LFP exhibits slow Li-ion transport during charging and discharging, thereby restricting its power density.[5−7]

According to classical diffusion theory, ionic transport within a single phase is governed by the concentration gradient of Li ions. However, in microsized LFP particles, such a pronounced concentration gradient is rare because two different (Li-rich and Li-deficient) phases coexist during (de)intercalation. These distinct phases exhibit an extremely limited solid-solution range and are subject to a two-phase reaction mechanism during (de)lithiation.[8] Triphylite $LiFePO_4$ crystallizes into an orthorhombic structure with space group *Pnma*. The crystal structure comprises corner-sharing FeO_6 octahedra and edge-sharing LiO_6 octahedra aligned along the *b*-axis and interconnected via PO_4 tetrahedra (Figure 1a,b). Upon full delithiation, $LiFePO_4$ transforms into the heterosite phase $FePO_4$, which preserves the orthorhombic *Pnma* framework but with oxidized Fe^{3+}. This transformation is accompanied by a lattice contraction along the a- and b- axes. In contrast, the corner-sharing FeO_6 octahedra and PO_4 tetrahedral framework remain topologically intact[9] (Tables 1 and2 and Figure 1c).

Ionic transport of Li during deintercalation has been modeled using the spinodal decomposition[10] and domino-cascade[11] models. Both models suggest that (de)lithiation proceeds through coordinated Li migration along the b-channel, governed by the propagation of phase boundaries or nucleation fronts. Unlike conventional intercalation electrodes, ionic transport in LFP is not controlled by the concentration gradient of the bulk material but by interface-driven phase transformation.[12] Consequently, the phase transformation of LFP is a key limiting factor in Li (de)intercalation because it induces a lattice mismatch and mechanical strain at the phase boundary.[13,14] This phase-boundary-controlled behavior constrains Li-ion transport in LFP and contributes to progressive structural degradation during long-term cycling.[15−18] Therefore, the power performance and cyclability of LFP can be

Received: February 4, 2026
Revised: March 21, 2026
Accepted: March 23, 2026
Published: April 6, 2026

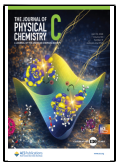

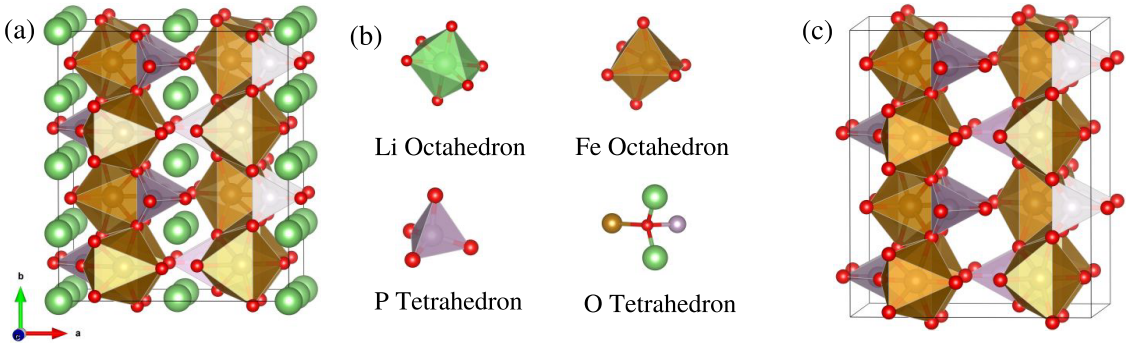

Figure 1. (a) Optimized crystal structure of $LiFePO_4$ viewed along the *c*-axis. (b) Local environments of Li, Fe, P and O. Li, O, P, and Fe atoms denoted as green, brown, purple, and red spheres, respectively. (c) Optimized crystal structure of fully delithiated $FePO_4$.

Table 1. Lattice Parameters and Unit Cell Volume for the Fully Lithiated States of LFP, LFPN, LFPS, and LFPNS, Calculated by DFT Using the PBE + *U* + D3 Method

	LFP	LFPN	LFPS	LFPNS
a [Å]	10.36	10.375	10.366	10.353
b [Å]	6.057	6.06	6.052	6.045
c [Å]	4.706	4.711	4.704	4.718
volume [Å^3]	295.304	296.192	295.106	295.301

Table 2. Lattice Parameters and Unit Cell Volume for the Fully Delithiated States of LFP, LFPN, LFPS, and LFPNS, Calculated by DFT Using the PBE + *U* + D3 Method

	LFP	LFPN	LFPS	LFPNS
a [Å]	9.880	9.921	9.916	9.918
b [Å]	5.887	5.884	5.868	5.863
c [Å]	4.863	4.847	4.843	4.828
volume [Å^3]	282.849	282.944	281.8	280.745

enhanced by developing a strain-tolerant LFP material that facilitates continuous Li-ion (de)intercalation through solid-solution transformation rather than abrupt phase separation.[19,20]

Over the years, diverse attempts have been made to enhance the electrochemical performance of the LFP electrode material. For example, a conductive coating of LFP particles was applied to create a conductive network that enhances electronic conductivity and suppresses Fe^{2+} oxidation or particle agglomeration.[21] LFP particle morphologies (nanoparticles, nanowires, nanosheets, and porous/hollow structures) have been controlled to shorten the Li-ion diffusion paths, increase surface contact with the electrolyte, and mitigate volume changes.[22] Novel binders, conductive additives, and fabrication techniques have been used to enhance mechanical stability, improve conductivity, and facilitate Li^+ transport.[23] Among these, substitutional cation doping has proven effective in enhancing the electrochemical performance of LFP. Replacing Fe with Ni or P with Si has improved structural stability and Li^+ transport kinetics.[1,24] However, codoping with Ni and Si has not yet been investigated. Such codoping is expected to further reduce the miscibility gap between the $LiFePO_4$ and $FePO_4$ phases, thereby introducing thermodynamically stable intermediate phases and suppressing abrupt phase separation by replacing the single two-phase reaction with sequential, staged transitions during (de)lithiation.

Herein, an extensive set of *density functional theory* (DFT) calculations are performed to investigate the influence of single- or codoping LFP with Ni and Si on the phase stability, structural evolution, electronic properties, and electrochemical characteristics of LFP during cycling. We demonstrate that although single-doped LFPs stabilize intermediate phases near the end of delithiation, codoping LFP with Ni and Si uniquely stabilizes multiple intermediate phases throughout the entire (de)lithiation process, replacing the single two-phase reaction with multiple sequential two-phase transitions and effectively mitigating abrupt phase separation. Moreover, Ni−Si codoping is shown to significantly reduce anisotropic lattice distortion, particularly suppressing *c*-axis expansion by approximately 1% during delithiation, thereby enhancing structural integrity during electrochemical cycling. Furthermore, the intercalation voltage is shown to increase, while the electronic band gap notably decreases in the case of Ni−Si codoped LFP, facilitating charge carrier generation and enhancing electronic transport in LFP. This study shows that Ni−Si codoping is an effective strategy for simultaneously enhancing the structural robustness, electrochemical performance, and rate capability of LFP.

2. COMPUTATIONAL METHODS

To describe the interaction between the core and valence electrons, spin-polarized DFT simulations were performed using the projector augmented-wave method.[25] To describe the exchange−correlation energy, the generalized gradient approximation (GGA) with the Perdew−Burke−Ernzerhof (PBE) functional was used.[26] The strong on-site Coulomb interactions of the localized Fe 3d orbitals were considered using GGA + *U* with an effective Hubbard *U* parameter of 5.3 eV.[27] The dispersion interaction were incorporated via the DFT-D3 method with Becke−Johnson damping.[28] The cutoff energy of the plane wave was set to 520 eV. An orthorhombic 1 × 2 × 2 supercell was constructed based on the *Pnma* space group containing 16 formula units. Structural optimization was considered completed when the total energy change between successive ionic steps was less than 0.00056 eV. A *γ*-centered 2 × 2 × 3 *k*-point mesh was used to sample the Brillouin zone.

Pristine LFP was simulated as well as that doped with Ni, Si, and both Ni and Si (Figure 2). The dopants were incorporated by placing isovalent Ni^{2+} dopants at the Fe sites and aliovalent Si^{4+} dopants at the P sites. The disordered alloy structures of $Li_{16}Fe_{15}NiP_{16}O_{64}$, $Li_{16}Fe_{16}P_{15}SiO_{64}$, and $Li_{16}Fe_{15}NiSiP_{15}O_{64}$ were created by a special quasi-random structure implemented in the alloy theory automated toolkit package.[29] Hereafter, the Ni-, Si-, and Ni−Si codoped LFPs are referred to as LFPN, LFPS, and LFPNS, respectively. The enumlib library of pymatgen[30] was used to enumerate various Li-vacancy orderings to prescreen the low-energy configurations of a partially lithiated state.[31−33] Fifty distinct lithium-vacancy orders were generated for each delithiation level. At each delithiation level, the ten configurations with the lowest classical electrostatic energies were

https://doi.org/10.1021/acs.jpcc.6c00767
J. Phys. Chem. C 2026, 130, 5369−5377

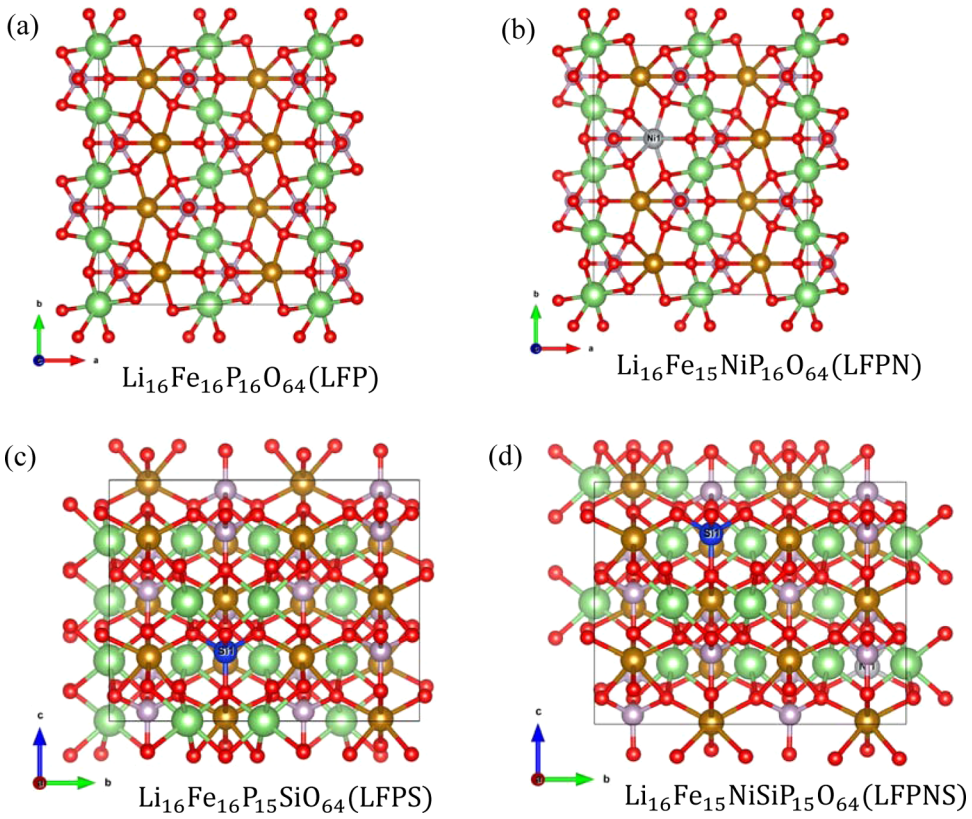

Figure 2. Relaxed structures of (a) pristine LFP and that doped with (b) Ni, (c) Si, and (d) both Ni and Si. Ni and Si are denoted as gray and blue spheres, respectively.

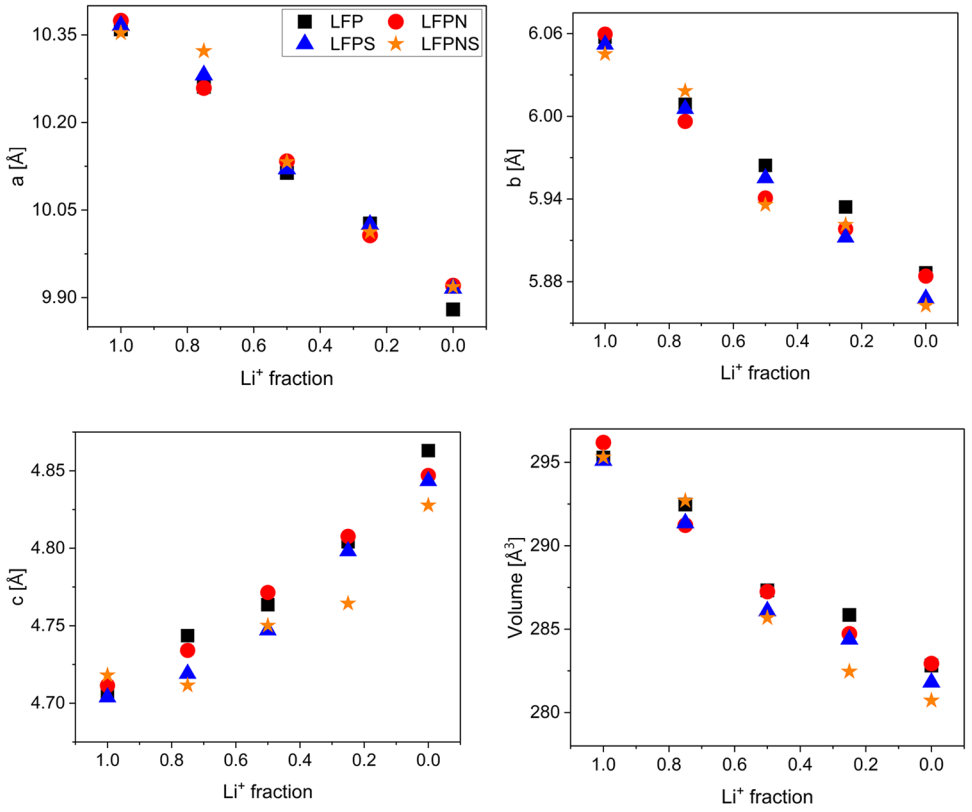

Figure 3. Variations in the lattice parameters (*a*, *b*, and *c*) and unit cell volume with delithiation for LFP, LFPN, LFPS, and LFPNS. Incorporating Ni and Si into the structure effectively suppresses the expansion of the *c* lattice parameter.

https://doi.org/10.1021/acs.jpcc.6c00767
J. Phys. Chem. C 2026, 130, 5369−5377

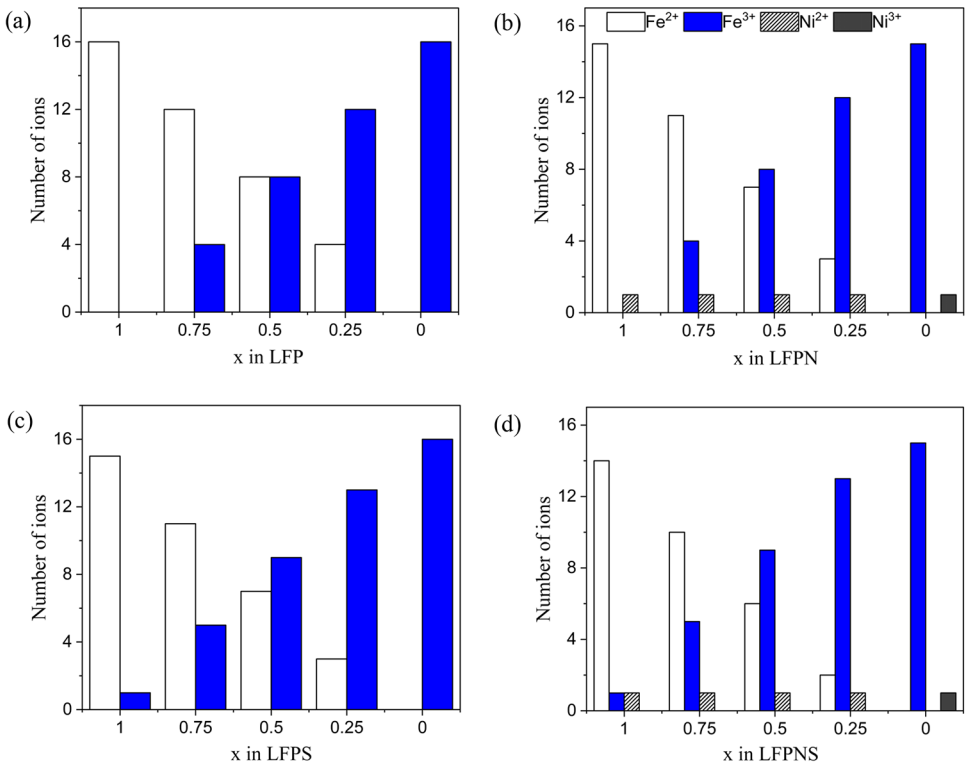

Figure 4. Oxidation states of transition-metal ions at various lithiation levels xs ($1 \geq x \geq 0$) for (a) pristine LFP ($Li_{16}Fe_{16}P_{16}O_{64}$), (b) LFPN ($Li_{16}Fe_{15}NiP_{16}O_{64}$), (c) LFPS ($Li_{16}Fe_{16}SiP_{15}O_{64}$), and (d) LFPNS ($Li_{16}Fe_{15}NiSiP_{15}O_{64}$).

selected. DFT calculations were subsequently performed on the prescreened configurations, and the most stable structure was identified for further analysis of thermodynamic stability and intercalation voltage. The oxidation states were determined via Bader charge analysis and corroborated by calculating the magnetic moments. All DFT methods were implemented using the Vienna Ab initio Simulation Package.[34,35]

3. RESULTS AND DISCUSSION

3.1. Structural Properties

Structural optimization of the pristine LFP yielded the following lattice parameters: a = 10.36 Å, b = 6.057 Å, and c = 4.706 Å, which corresponded to a unit cell volume of 295.304 Å^3. These values agree well with previous experimental reports.[36−38] The X-ray diffraction pattern of the optimized structure (Figure S1) also matched experimental data.[39] The fully lithiated state of LFPN had larger lattice parameters and unit cell volume than those of pristine LFP (Table 1), despite the fact that Ni^{2+} has a smaller radius (~0.69 Å) than Fe^{2+} (~0.78 Å). This counterintuitive expansion arises from the local lattice distortion induced by Ni substitution at the Fe site. The electronic structure modification and increased Ni−O bond strength led to anisotropic expansion along a specific crystallographic direction, which is consistent with a previous study.[40] In contrast, LFPS and LFPNS had lattice parameters and unit cell volumes comparable to those of pristine LFP, indicating that Si substitution at the P site did not disturb the PO tetrahedral framework.

With the full delithiation of pristine LFP, $LiFePO_4$ transformed into the heterosite $FePO_4$ while preserving the overall olivine framework. The lattice parameters of $FePO_4$ were a = 9.88 Å, b = 5.887 Å, and c = 4.863 Å, producing a unit cell volume of 282.849 Å^3. This transformation corresponds to a 4.22% decrease in volume; 4.63% and 2.81% contractions in the a and b parameters, respectively; and a 3.34% expansion along the c-axis (Table 2 and Figure 3).

Figure 3 shows the structural distortions of LFP, LFPN, LFPS, and LFPNS during progressive delithiation. All LFPs exhibit a similar trend: extracting Li^+ decreases the unit cell volume and lattice parameters a and b but increases the lattice parameter c. However, quantitative differences among the doped systems reveal the impact of substitutional cations on the structural response. In the case of a fully lithiated state, Ni substitution at the Fe site of LFPN leads to anisotropic expansions along the a, b, and c axes, whereas Si substitution at the P site has a minimal effect on the intrinsic structure of LFP. As presented in Tables 1 and 2, the changes in the a and c parameters during LFPNS delithiation (4.2% and 2.3%, respectively) were smaller than those of pristine LFP (4.6% and 3.3%, respectively). In particular, for LFPNS, expansion along the c-axis was reduced by approximately 1%, indicating mitigated structural distortion during electrochemical cycling. Although the overall volume change of LFPNS under full delithiation is the greatest observed herein, it originates from the suppressed c-axis expansion, and the in-plane (a−b) contraction remains comparable to that of the undoped and other doped structures, thereby preserving structural integrity (Figure 3). The moderated lattice responses of LFPNS presumably allow for a gradual and continuous evolution of the cell parameters without abrupt changes, thus, reducing internal stress accumulation and contributing to improved structural stability. Overall, the comparison highlights that Ni and Si doping, particularly in combination, effectively moderates lattice distortions and fosters uniform structural evolution during Li^+ extraction.

https://doi.org/10.1021/acs.jpcc.6c00767
J. Phys. Chem. C 2026, 130, 5369−5377

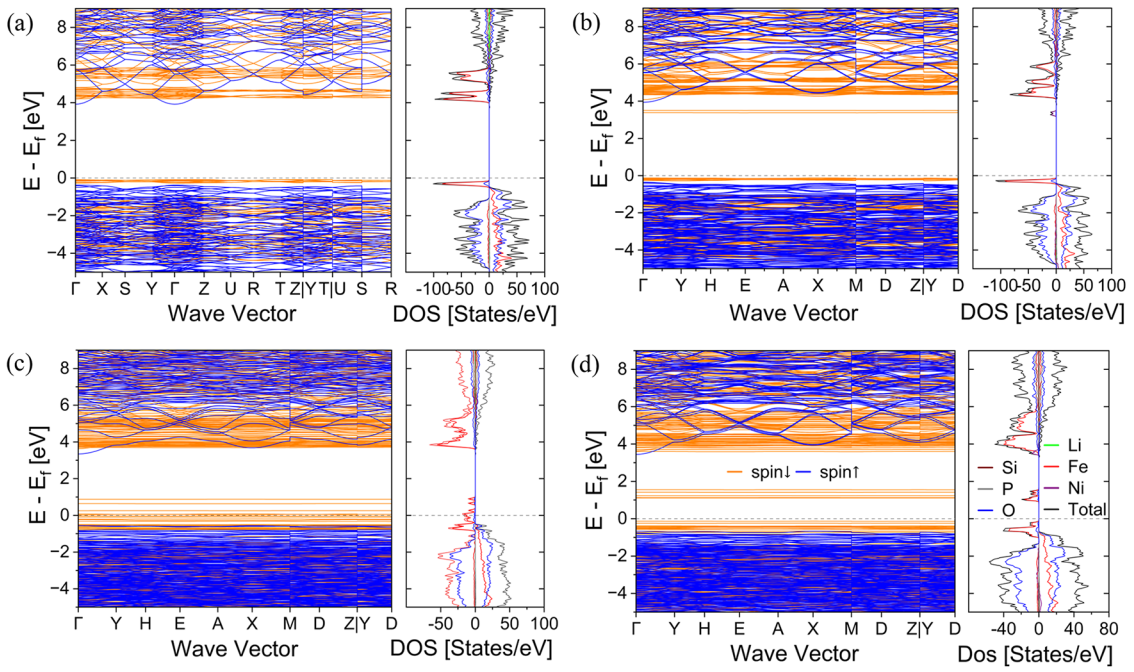

Figure 5. Spin-polarized band structures and corresponding DOS for (a) pristine LFP, (b) Ni-doped LFPN, (c) Si-doped LFPS, and (d) Ni−Si codoped LFPNS. In all cases, the Fermi level is set to zero.

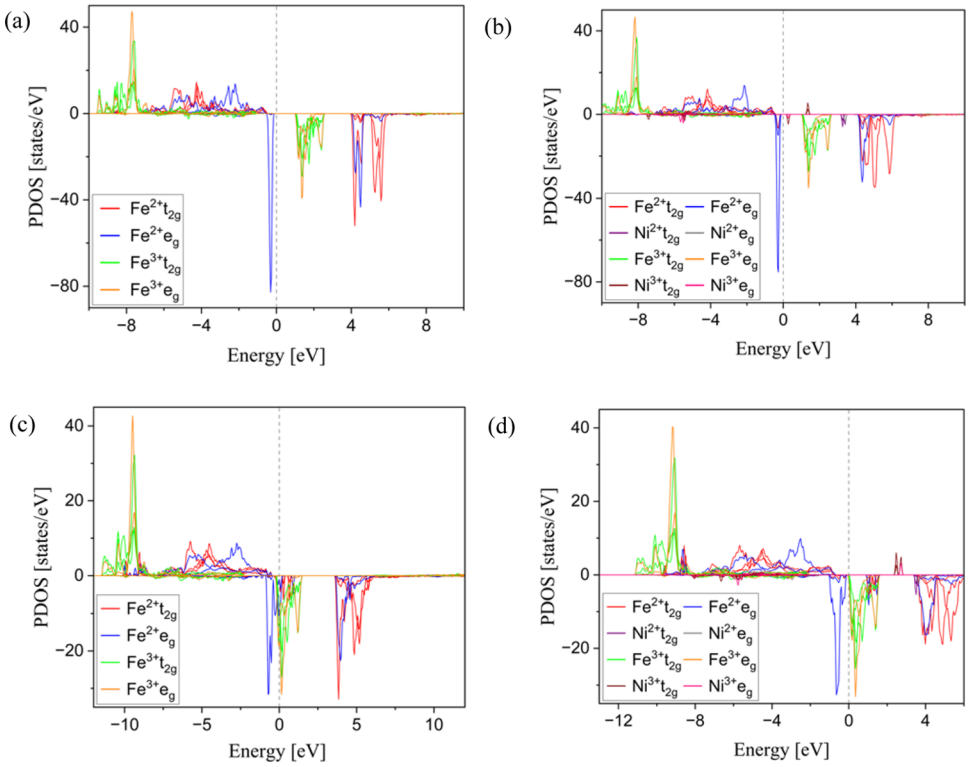

Figure 6. PDOS of (a) pristine LFP, (b) Ni-doped LFPN, (c) Si-doped LFPS, and (d) Ni−Si codoped LFPNS. In each panel, the PDOS of Fe^{2+} and Ni^{2+} (Fe^{3+} and Ni^{3+}) refer to the fully lithiated (delithiated) state.

3.2. Electronic Structure and Redox Behavior

The redox behaviors of the present LFPs were investigated by examining the oxidation states of the transition-metal ions at various lithiation levels (Figure 4). For pristine LFP, the primary redox-active species during cycling is the Fe^{2+}/Fe^{3+} redox couple. In the fully lithiated state (x = 1), no Fe^{3+} is present in LFP or LFPN. However, in the cases of LFPS and LFPNS, approximately 6.3% Fe^{3+} is present, even in the fully lithiated state. This can be explained by the fact that the substitution of Si^{4+} for P^{5+} introduces a charge imbalance that is locally compensated for by the oxidation of Fe^{2+} to Fe^{3+}. Incorporating Si^{4+} into LFPS and LFPNS enhances their structural stability owing to the stronger Fe^{3+}−O bonds relative to the Fe^{2+}−O bonds. Moreover, the greater radius of

https://doi.org/10.1021/acs.jpcc.6c00767
J. Phys. Chem. C 2026, 130, 5369−5377

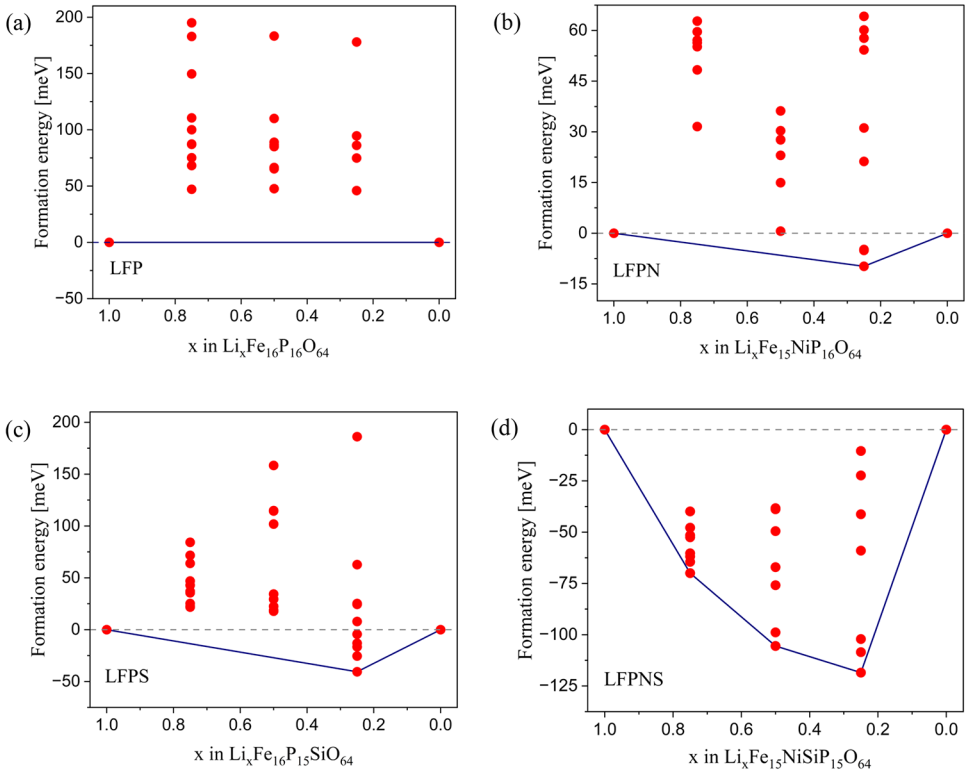

Figure 7. Formation energies calculated via DFT for various Li^+ vacancy orderings (red circles) calculated for (a) pristine LFP, (b) Ni-doped LFPN, (c) Si-doped LFPS, and (d) Ni−Si codoped LFPNS. In each panel, the convex hull is denoted by a sold line.

Si^{4+} (0.26 Å) compared to P^{5+} (0.17 Å) induces a slight expansion of the local SiO_4 tetrahedron. This structural distortion relaxes local strain and, in turn, mitigates volume changes during the repeated lithiation/delithiation cycles. In addition, preoxidation of a fraction of Fe^{2+} to Fe^{3+} reduces the concentration of Jahn−Teller-active Fe^{2+}, thereby suppressing lattice distortion and improving structural integrity over prolonged cycling. However, the oxidation of Fe^{2+} to Fe^{3+} for charge compensation prior to delithiation restricts the amount of redox-active Fe^{2+} available during electrochemical cycling. Because Fe^{3+} cannot be further oxidized under normal operating conditions, the presence of preoxidized Fe^{3+} leads to a reduction in theoretical capacity. Therefore, optimizing the concentration of Si^{4+} dopants appear critical for achieving structural stabilization without significantly compromising the electrochemical capacity of LFP. In contrast to Si doping, Ni doping has little effect on the redox behavior of LFP, other than the emergence of a small fraction of Ni^{3+} in the final stage of delithiation.

Figure 5 shows the spin-polarized band structures and *density of states* (DOS) of the pristine and doped LFPs. For pristine LFP (Figure 5a), both the *valence band maximum* and *conduction band minimum* (CBM) are primarily composed of Fe 3d orbitals, yielding a band gap of 3.9 eV, which is in agreement with the reported value of 3.8 eV.[41] Ni doping (Figure 5b) introduces localized spin-down Ni 3d states just below the CBM, reducing the band gap to 3.4 eV. In contrast, Si doping (Figure 5c) induces a downward shift of the spin-down P 3p-derived states near the Fermi level, significantly narrowing the band gap to 0.07 eV. In the case of Ni−Si codoping (Figure 5d), the band gap is 1.2 eV, which is smaller than that of pristine LFP but larger than that of pure Si doping. This partial reopening of the gap arises from the competing electronic effects of the Ni 3d- and Si-induced P 3p states, with band edges predominantly governed by Fe 3d orbitals, indicating a moderated electronic perturbation relative to pure Si doping. The largely flat band dispersions observed for both pristine and doped LFPs suggest strong carrier localization, which is consistent with small-polaron-type transport.

The charge transport of an insulating or weakly conducting transition-metal oxide is predominantly governed by a small-polaron hopping mechanism rather than band-like transport.[9] A small polaron forms when a change in the valence state of a transition-metal ion induces local lattice distortion, leading to carrier localization. In olivine $LiFePO_4$, Li^+ extraction produces excess charge carriers in the form of localized hole polarons associated with the Fe^{2+}/Fe^{3+} redox couple. Electronic transport is therefore dominated by the thermally activated hopping of these polarons between neighboring Fe sites. In this context, the band gap reduction induced by Si- and Ni−Si codoping has the potential to lower the activation energy for carrier hopping between Fe^{2+}/Fe^{3+} sites, thereby enhancing electronic conductivity.

As shown in Figure 6, the *projected* DOS (PDOS) elucidates the influence of doping on the electronic structure of LFP. In the fully lithiated LFP, Fe^{2+} 3d orbitals dominate near the Fermi level, indicating their significant contribution to the electronic properties of the material. Upon delithiation, Fe^{3+} states emerge in the band gap, forming a new CBM and marking a clear shift in the electronic structure associated with oxidation. All four PDOS diagrams in Figure 6 reveal a distinct and symmetrical crystal field splitting of the Fe 3d orbitals into t_{2g} and e_g subsets, which is characteristic of octahedral coordination of the Fe ion. The observed splitting pattern, along with the magnetic moments calculated from spin-polarized self-consistent field calculations, suggests that the Fe

https://doi.org/10.1021/acs.jpcc.6c00767
J. Phys. Chem. C 2026, 130, 5369−5377

ions adopted high-spin configurations. Specifically, Fe^{2+} exhibits an electron configuration of $t_{2g}^4(\uparrow\downarrow|\uparrow|\uparrow)$ $e_g^2(\uparrow|\uparrow)$, while that of Fe^{3+} is $t_{2g}^3(\uparrow|\uparrow|\uparrow)$ $e_g^2(\uparrow|\uparrow)$. Similarly, the PDOS of the Ni- and Ni−Si codoped LFPs reveal electronic configurations consistent with the high-spin Ni^{2+} and Ni^{3+} states. Ni^{2+} is characterized by a configuration of $t_{2g}^6(\uparrow\downarrow|\uparrow\downarrow|\uparrow\downarrow)$ $e_g^2(\uparrow|\uparrow)$, while that of Ni^{3+} is $t_{2g}^5(\uparrow\downarrow|\uparrow\downarrow|\uparrow)$ $e_g^2(\uparrow|\uparrow)$. These findings highlight the retention of high-spin character across both Fe and Ni ions, reinforcing the interpretation that the dopants preserve the local electronic structure symmetry while modifying the electronic states near the Fermi level.

3.3. Thermodynamic Stability and Intercalation Voltage

The formation reaction for a partially lithiated state is given in eq 1.

$$x\mathrm{LiFePO_4} + (1 - x)\mathrm{FePO_4} \rightarrow \mathrm{Li}_x\mathrm{FePO_4} \quad (1)$$

The thermodynamic stability of the partially (de)lithiated state was evaluated using the formation energy E_f, defined in eq 2.

$$E_f = E(\mathrm{Li}_x\mathrm{FePO_4}) - xE(\mathrm{LiFePO_4}) - (1 - x)E(\mathrm{FePO_4}) \quad (2)$$

where $E(\mathrm{Li}_x\mathrm{FePO_4})$, $E(\mathrm{LiFePO_4})$, and $E(\mathrm{FePO_4})$ represent the energies of the partially lithiated, fully lithiated, and fully delithiated states, respectively. For a given x, $E(\mathrm{Li}_x\mathrm{FePO_4})$ was obtained by identifying the lowest-energy configuration among various lithium-vacancy arrangements, as illustrated in Figure 7. The formation energies of $\mathrm{Li}_x\mathrm{FePO_4}$ (pristine LFP) are positive across all lithium-vacancy configurations (denoted by circles), indicating that all intermediate compositions lie above the convex hull. This is consistent with previous computational and experimental studies that support the two-phase reaction mechanism throughout the full range of (de)lithiation.[20,42,43]

In contrast to pristine LFP, doped LFP shows a negative minimum in formation energy, indicating the formation of thermodynamically stable intermediate phases, specifically the formation of a superstructure in a partially (de)lithiated state. In the cases of LFPN and LFPS, thermodynamically stable intermediate phases are present in the range $0.25 \geq x \geq 0$. This suggests that the single two-phase reaction of pristine LFP is partially replaced by sequential two-phase transitions through stable intermediate compositions lying on the convex hull near the fully delithiated state. In the Ni−Si codoped system (LFPNS), the effect of codoping is even more pronounced (Figure 7d). The formation energies are negative across the entire range of (de)lithiation, indicating the existence of multiple thermodynamically stable intermediate phases, as evidenced by intermediate compositions lying on the convex hull throughout (de)lithiation. Rather than a single two-phase reaction as in pristine LFP, LFPNS undergoes multiple sequential two-phase transitions through these stable intermediate compositions. This behavior is highly beneficial for the high-rate performance and power-demanding applications of LFPNS, where rapid and reversible Li^+ insertion and extraction is critical.

From the convex hulls derived for the pristine and doped LFPs (Figure 7), corresponding voltage profiles were constructed by using eqs 3 and 4.

$$\mathrm{Li}_x\mathrm{FePO_4} + \mathrm{d}x\mathrm{Li} \rightleftharpoons \mathrm{Li}_{x+\mathrm{d}x}\mathrm{FePO_4} \quad (3)$$

$$V = -\frac{E(\mathrm{Li}_{x+\mathrm{d}x}\mathrm{FePO_4}) - E(\mathrm{Li}_x\mathrm{FePO_4}) - \mathrm{d}x.E(\mathrm{Li})}{\mathrm{d}x.e} \quad (4)$$

where $\mathrm{d}x$ denotes the amount of incremental delithiation, $E(\mathrm{Li})$ is the reference energy of metallic lithium, and e is the elementary charge. Because the PBE functional systematically overestimates the intercalation voltage, a correction factor of 0.6 V was subtracted to align the calculated voltages with the experimental values.

As shown in Figure 8, the voltage plateau of LFP from the PBE + U calculation is approximately 3.48 V, which agrees well

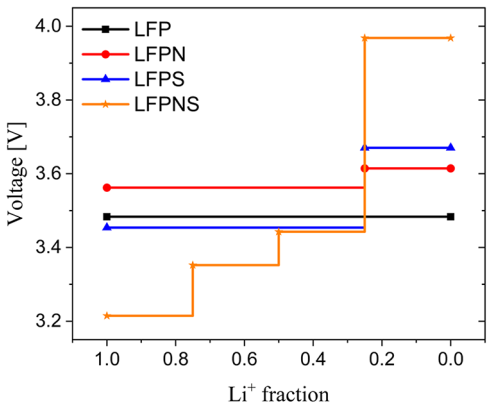

Figure 8. Voltage profiles of pristine LFP, Ni-doped LFPN, Si-doped LFPS, and Ni−Si codoped LFPNS at various lithiation levels.

with previous experimental and first-principles studies.[44−47] This well-defined plateau reflects the characteristic two-phase reaction mechanism during Li (de)intercalation in which the $\mathrm{LiFePO_4}$ and $\mathrm{FePO_4}$ phases coexist without forming intermediate solid-solution states.

In contrast, the doped LFPs exhibit notable deviations from the flat behavior of the LFP. Specifically, for the Ni-doped (LFPN) and Si-doped (LFPS) systems, the deintercalation voltage progressively increases toward the end of the delithiation process. The flat voltage plateau is replaced by a sloped voltage profile because of the stabilization of the intermediate Li compositions. In the case of LFPNS, the deviation is even more pronounced: The deintercalation voltage exhibits multiple distinct plateaus spanning the entire delithiation range, consistent with multiple sequential two-phase reactions through stable intermediate compositions, as evidenced by the multivertex convex hull in Figure 7d. This behavior is consistent with the thermodynamic stabilization of the intermediate states of the LFPNS discussed above. Furthermore, the average intercalation voltages of all doped systems are higher than those of pristine LFP (3.48 V). The average voltages are 3.57 V for LFPN (representing a 2.5% increase), 3.50 V for LFPS (0.5% increase), and 3.49 V for LFPNS (0.3% increase). These voltage enhancements not only reflect improved thermodynamic stability but also suggest potential benefits for energy density and high-voltage operation in battery applications.

4. CONCLUSION

The cathode material (LFP) undergoes phase separation into Li-rich and Li-poor regions during the (de)charging process, forming a two-phase system. This phase separation imposes fundamental limitations on the high-rate performance of LFP owing to mechanical strain and sluggish phase-boundary movement. Suppression of this two-phase behavior is crucial for high-power applications of LFP. Using first-principles

https://doi.org/10.1021/acs.jpcc.6c00767
J. Phys. Chem. C 2026, 130, 5369−5377

calculations, we evaluated the phase stabilities of LFPs doped with Ni and Si by evaluating the formation energies of partially (de)lithiated states. We observed the formation of thermodynamically stable intermediate phases near the end of the (de)lithiation process for single-doped LFP (with Ni or Si), indicative of sequential two-phase transitions replacing the single two-phase reaction near full delithiation. More notably, LFP codoped with Ni and Si exhibited multiple thermodynamically stable intermediate phases throughout the entire (de)lithiation range, resulting in a staged delithiation mechanism via multiple sequential two-phase reactions. The Ni−Si codoped LFP also exhibited reduced lattice expansion of approximately 1% along the *c*-axis, mitigating structural distortion during electrochemical cycling. The present doping method also yielded an enhanced average voltage with a sloped profile. Moreover, the band gap was considerably reduced by Si- and Ni−Si codoping, which facilitated carrier generation and electronic transport. These findings collectively underscore the effectiveness of Ni−Si codoping in improving both the structural stability and electrochemical performance of LFP cathode material for high-rate LIB applications.

■ ASSOCIATED CONTENT

Supporting Information

The Supporting Information is available free of charge at https://pubs.acs.org/doi/10.1021/acs.jpcc.6c00767.

Lattice parameters *a*, *b*, and *c* (Å) and volume in (Å^3) of the pristine and doped LFPs (Table S1); Bader charges and oxidation states of the 16 transition-metal ions of the pristine and doped LFPs (Table S2); voltage profiles of the pristine and doped LFPs (Table S3); X-ray diffraction patterns of the pristine and doped LFPs (Figure S1) (PDF)

■ AUTHOR INFORMATION

Corresponding Authors

Mengdi Zhao − *Department of Materials Science and Engineering, Suzhou University of Science and Technology, Suzhou 215009, People's Republic of China*; Email: mdzhao@usts.edu.cn

Joonkyung Jang − *Department of Nanoenergy Engineering, Pusan National University, Busan 46241, Republic of Korea*; orcid.org/0000-0001-9028-0605; Phone: +82-51-510-3983; Email: jkjang@pusan.ac.kr

Authors

Yelak F. Abebe − *Department of Nanoenergy Engineering, Pusan National University, Busan 46241, Republic of Korea*; orcid.org/0000-0002-0164-1841

Arindam Sannyal − *Department of Nanoenergy Engineering, Pusan National University, Busan 46241, Republic of Korea*; orcid.org/0000-0002-8376-7017

Kisang Byun − *Department of Nanoenergy Engineering, Pusan National University, Busan 46241, Republic of Korea*; orcid.org/0000-0001-6648-2792

Complete contact information is available at: https://pubs.acs.org/10.1021/acs.jpcc.6c00767

Author Contributions

Y.F.A.: Conceptualization, investigation, software, writing—original draft, and visualization. A.S.: Investigation, software, and validation. K.B.: Investigation, software, and visualization. M.Z: Writing—review and editing. J.J: Validation, writing—original draft, writing—review and editing, supervision, and project administration.

Notes

The authors declare no competing financial interest.

■ ACKNOWLEDGMENTS

This work was supported by the Industrial Technology Innovation Program (RS-2024-00435432: Development of hydrogen production technology through ammonia decomposition using a plasmonics-based light system with high performance and long-term durability), funded by the Ministry of Trade Industry & Energy (MOTIE, Korea).

■ ABBREVIATIONS

LFP, lithium iron phosphate; LIB, lithium-ion battery; DFT, density functional theory; GGA, generalized gradient approximation; PBE, Perdew−Burke−Ernzerhof; LFPN, Ni-doped LFP; LFPS, Si-doped LFP; LFPNS, Ni−Si codoped LFP; CBM, conduction band minimum; DOS, density of states; PDOS, projected density of states

■ REFERENCES

(1) Akhmetova, K.; Sultanov, F.; Mentbayeva, A.; Umirov, N.; Bakenov, Z.; Tatykayev, B. Advances in multi-element doping of LiFePO4 cathode material for capacity enhancement in Li-ion batteries. *J. Power Sources* **2024**, *624*, No. 235531.

(2) Jiang, X.; Xin, Y.; He, B.; Zhang, F.; Tian, H. Effect of Heteroatom Doping on Electrochemical Properties of Olivine LiFePO4 Cathodes for High-Performance Lithium-Ion Batteries. *Materials* **2024**, *17* (6), No. 1299.

(3) Lv, Z.; Li, M.; Yang, H.; Lin, J.; Luo, J.; Hong, R.; Wu, B.; Cao, S. C. The first-principles study on electrochemical performance, mechanical properties, and lithium-ion migration of LiFePO4 modified by doping with Co and Nb. *J. Solid State Electrochem.* **2024**, *28* (8), 2873−2883.

(4) Zhou, G.; Wang, P.; Li, Z.; Li, Y.; Yao, Y. Revealing electrochemical performance of Ni doping LiFePO4 composite. *Bull. Mater. Sci.* **2024**, *47* (4), No. 251.

(5) Bo, Z.; Yufang, H.; Hongqiang, G.; Xiaodan, W.; Jinli, L.; Hong, X.; Li, W.; Xiangming, H. Unraveling the doping mechanisms in lithium iron phosphate. *Energy Mater.* **2022**, *2*, No. 200013.

(6) Liu, Q.; Wen, D.; Yu, X.; Jiang, H. Effect of Na-Si co-doping on the performance of LiFePO4. *J. Electroanal. Chem.* **2023**, *950*, No. 117891.

(7) Wang, Z.; Kong, X.; Fan, Z.; Ding, S.; Rong, Q.; Su, Y. A First-Principles Study of Anion Doping in LiFePO4 Cathode Materials for Li-Ion Batteries. *ChemPhysChem* **2024**, *25* (3), No. e202300756.

(8) Srinivasan, V.; Newman, J. Discharge Model for the Lithium Iron-Phosphate Electrode. *J. Electrochem. Soc.* **2004**, *151* (10), A1517−A1529.

(9) Banday, A.; Shahid, R.; Gupta, M.; Murugavel, S. Tunable electronic structure of heterosite FePO(4): an in-depth structural study and polaron transport. *RSC Adv.* **2023**, *13* (27), 18332−18346.

(10) Ramana, C. V.; Mauger, A.; Gendron, F.; Julien, C. M.; Zaghib, K. Study of the Li-insertion/extraction process in LiFePO4/FePO4. *J. Power Sources* **2009**, *187* (2), 555−564.

(11) Delmas, C.; Maccario, M.; Croguennec, L.; Le Cras, F.; Weill, F. Lithium deintercalation in LiFePO4 nanoparticles via a domino-cascade model. *Nat. Mater.* **2008**, *7* (8), 665−671.

(12) Zhang, W.-J. Structure and performance of LiFePO4 cathode materials: A review. *J. Power Sources* **2011**, *196* (6), 2962−2970.

(13) Peng, J.; Li, Z.; You, Y.; Liu, J.; Wang, L.; Xu, J.; Ou, S.; Yuan, M. Contribution of Ti-Doping to the Cyclic Stability of LiFe0.6-Mn0.4PO4/C. *Ind. Eng. Chem. Res.* **2024**, *63* (18), 8228−8238.

(14) Ramar, V.; Pszolla, C.; Weinberger, M.; Borck, M.; Zinck, L. Electrochemical Kinetics of LiFePO4 Cathode Material in Non-flammable Inorganic Liquid Electrolyte. *ChemSusChem* **2025**, *18* (2), No. e202400122.
(15) Chen, J.; Wang, F.; Yin, M.; Yao, C. First-Principles Study on the Electronic Properties and Mechanical Stabilities of Anion-Cation Multiple-Doped LiFePO4. *ChemistrySelect* **2022**, *7* (38), No. e202202834.
(16) Kumar, A.; Thomas, R.; Karan, N.; Saavedra-Arias, J.; Singh, M.; Majumder, S.; Tomar, M.; Katiyar, R. Structural and Electrochemical Characterization of Pure LiFePO4 and Nanocomposite C-LiFePO4 Cathodes for Lithium Ion Rechargeable Batteries. *J. Nanotechnol.* **2009**, *2009*, No. 176517, DOI: 10.1155/2009/176517.
(17) Liu, Y.; Qin, W.; Zhang, D.; Feng, L.; Wu, L. Effect of Na+ in situ doping on LiFePO4/C cathode material for lithium-ion batteries. *Prog. Nat. Sci.: Mater. Int.* **2021**, *31* (1), 14−18.
(18) Nakayama, M.; Yamada, S.; Jalem, R.; Kasuga, T. Density functional studies of olivine-type LiFePO4 and NaFePO4 as positive electrode materials for rechargeable lithium and sodium ion batteries. *Solid State Ionics* **2016**, *286*, 40−44.
(19) Sgroi, M. F.; Lazzaroni, R.; Beljonne, D.; Pullini, D. Doping LiMnPO4 with Cobalt and Nickel: A First Principle Study. *Batteries* **2017**, *3* (2), No. 11.
(20) Yamada, A.; Koizumi, H.; Nishimura, S.-i.; Sonoyama, N.; Kanno, R.; Yonemura, M.; Nakamura, T.; Kobayashi, Y. Room-temperature miscibility gap in LixFePO4. *Nat. Mater.* **2006**, *5* (5), 357−360.
(21) Wang, L.; Chen, H.; Zhang, Y.; Liu, J.; Peng, L. Research Progress in Strategies for Enhancing the Conductivity and Conductive Mechanism of LiFePO4 Cathode Materials. *Molecules* **2024**, *29* (22), No. 5250.
(22) Okada, K.; Kimura, I.; Machida, K. High rate capability by sulfur-doping into LiFePO4 matrix. *RSC Adv.* **2018**, *8* (11), 5848−5853.
(23) Chen, T.; Li, M.; Bae, J. Recent Advances in Lithium Iron Phosphate Battery Technology: A Comprehensive Review. *Batteries* **2024**, *10* (12), No. 424.
(24) Zhang, H.; Zou, Z.; Zhang, S.; Liu, J.; Zhong, S. A review of the Doping Modification of LiFePO4 as a Cathode Material for Lithium Ion Batteries. *Int. J. Electrochem. Sci.* **2020**, *15* (12), 12041−12067.
(25) Blöchl, P. E. Projector augmented-wave method. *Phys. Rev. B* **1994**, *50* (24), No. 17953.
(26) Perdew, J. P.; Burke, K.; Ernzerhof, M. Generalized Gradient Approximation Made Simple. *Phys. Rev. Lett.* **1996**, *77* (18), No. 3865.
(27) Timrov, I.; Marzari, N.; Cococcioni, M. HP − A code for the calculation of Hubbard parameters using density-functional perturbation theory. *Comput. Phys. Commun.* **2022**, *279*, No. 108455.
(28) Grimme, S.; Antony, J.; Ehrlich, S.; Krieg, H. A consistent and accurate ab initio parametrization of density functional dispersion correction (DFT-D) for the 94 elements H-Pu. *J. Chem. Phys.* **2010**, *132* (15), No. 154104, DOI: 10.1063/1.3382344.
(29) van de Walle, A.; Tiwary, P.; de Jong, M.; Olmsted, D. L.; Asta, M.; Dick, A.; Shin, D.; Wang, Y.; Chen, L. Q.; Liu, Z. K. Efficient stochastic generation of special quasirandom structures. *Calphad* **2013**, *42*, 13−18.
(30) Ong, S. P.; Richards, W. D.; Jain, A.; Hautier, G.; Kocher, M.; Cholia, S.; Gunter, D.; Chevrier, V. L.; Persson, K. A.; Ceder, G. Python Materials Genomics (pymatgen): A robust, open-source python library for materials analysis. *Comput. Mater. Sci.* **2013**, *68*, 314−319.
(31) Hart, G. L. W.; Forcade, R. W. Algorithm for generating derivative structures. *Phys. Rev. B* **2008**, *77* (22), No. 224115.
(32) Hart, G. L. W.; Nelson, L. J.; Forcade, R. W. Generating derivative structures at a fixed concentration. *Comput. Mater. Sci.* **2012**, *59*, 101−107.
(33) Morgan, W. S.; Hart, G. L. W.; Forcade, R. W. Generating derivative superstructures for systems with high configurational freedom. *Comput. Mater. Sci.* **2017**, *136*, 144−149.
(34) Kresse, G.; Furthmüller, J. Efficient iterative schemes for ab initio total-energy calculations using a plane-wave basis set. *Phys. Rev. B* **1996**, *54* (16), No. 11169.
(35) Kresse, G.; Joubert, D. From ultrasoft pseudopotentials to the projector augmented-wave method. *Phys. Rev. B* **1999**, *59* (3), No. 1758.
(36) Liu, Y.; Gu, Y.-J.; Luo, G.-Y.; Chen, Z.-L.; Wu, F.-Z.; Dai, X.-Y.; Mai, Y.; Li, J.-Q. Ni-doped LiFePO4/C as high-performance cathode composites for Li-ion batteries. *Ceram. Int.* **2020**, *46* (10, Part A), 14857−14863.
(37) Tang, P.; Holzwarth, N. Electronic structure of FePO4, LiFePO4, and related materials. *Phys. Rev. B* **2003**, *68*, No. 165107.
(38) Xu, J.; Chen, G. Effects of doping on the electronic properties of LiFePO4: A first-principles investigation. *Phys. B* **2010**, *405* (3), 803−807.
(39) Guo, B.; Ruan, H.; Zheng, C.; Fei, H.; Wei, M. Hierarchical LiFePO4 with a controllable growth of the (010) facet for lithium-ion batteries. *Sci. Rep.* **2013**, *3* (1), No. 2788.
(40) Nayak, C.; Bhasin, V.; Halankar, K. K.; Banerjee, S.; Bute, A.; Jha, S. N.; Bhattacharyya, D. Operando X ray absorption spectroscopy elucidating the de-lithiation/lithiation mechanism of Mn and Ni co-doped LiFePO4 cathodes. *J. Electroanal. Chem.* **2024**, *969*, No. 118536.
(41) Ban, C.; Yin, W.-J.; Tang, H.; Wei, S.-H.; Yan, Y.; Dillon, A. C. A Novel Codoping Approach for Enhancing the Performance of LiFePO4 Cathodes. *Adv. Energy Mater.* **2012**, *2* (8), 1028−1032.
(42) Zhou, F.; Cococcioni, M.; Marianetti, C. A.; Morgan, D.; Ceder, G. First-principles prediction of redox potentials in transition-metal compounds with LDA+U. *Phys. Rev. B* **2004**, *70* (23), No. 235121.
(43) Zhou, F.; Maxisch, T.; Ceder, G. Configurational Electronic Entropy and the Phase Diagram of Mixed-Valence Oxides: The Case of LiFePO4. *Phys. Rev. Lett.* **2006**, *97* (15), No. 155704.
(44) Timrov, I.; Aquilante, F.; Cococcioni, M.; Marzari, N. Accurate Electronic Properties and Intercalation Voltages of Olivine-Type Li-Ion Cathode Materials from Extended Hubbard Functionals. *PRX Energy* **2022**, *1* (3), No. 033003.
(45) Prosini, P. P. Modeling the Voltage Profile for LiFePO4. *J. Electrochem. Soc.* **2005**, *152*, No. A1925.
(46) Zhang, Y.; Alarco, J. A.; Best, A. S.; Snook, G. A.; Talbot, P. C.; Nerkar, J. Y. Re-evaluation of experimental measurements for the validation of electronic band structure calculations for LiFePO(4) and FePO(4). *RSC Adv.* **2019**, *9* (2), 1134−1146.
(47) Zhou, F.; Cococcioni, M.; Kang, K.; Ceder, G. The Li intercalation potential of LiMPO4 and LiMSiO4 olivines with M== Fe, Mn, Co, Ni. *Electrochem. Commun.* **2004**, *6* (11), 1144−1148.

https://doi.org/10.1021/acs.jpcc.6c00767
J. Phys. Chem. C 2026, 130, 5369−5377